Artificial Dielectric Devices for Variable Polarization Compensation at Millimeter and Submillimeter Wavelengths

Timothy D. Drysdale, Richard J. Blaikie, *Member, IEEE*, Harold M. H. Chong, and David R. S. Cumming, *Member, IEEE*

Abstract—Variable polarization compensation has been demonstrated at 100 GHz. The device consists of two interlocking V-groove artificial dielectric gratings that produce a birefringence that varies with the separation distance. A maximum retardance of 74 ° has been obtained experimentally in a silicon device, in good agreement with rigorous coupled-wave computer simulations. Further simulations predict that adding quarter wave dielectric antireflection (AR) coatings to the outer surfaces of the device can reduce the insertion loss to below 4 dB. The use of rectangular grooved gratings provides increased retardance and reduced loss. It is predicted that a coupled device with a rectangular grooved gratings will be capable of maximum retardance in excess of 180°, with low insertion loss (<0.6 dB). The sensitivity of the wave retardation as a function of mechanical separation has a peak value of 485°/mm. The design and micromachining fabrication techniques scale for operation at submillimeter wavelengths.

Index Terms—Anisotropic media, birefringence, compensation, micromachining, microwave measurements, millimeter wave devices, polarization, submillimeter wave devices.

I. INTRODUCTION

THERE is a rapidly growing interest in using millimeter and submillimeter wavelength systems for a variety of applications, such as near- and far-field imaging [1], [2], communications [3], spectroscopy [4], and investigation of physical phenomena [5]. Additionally, micromachined structures are of increasing importance in optics [6]. Aspects of polarization control must be addressed for many of these applications; with efficient polarization control, millimeter and submillimeter applications can enjoy benefits like those being gained at optical wavelengths, such as increased capacity in long span fiber optics from the elimination of polarization mode dispersion [7], and the use of polarization as a diversity or coding variable in communications systems [8]–[10]. Variable polarization compensators are well known in classical optics [11], where the polarization is varied by altering the path length through a fixed-birefringence crystal such as calcite, or electrically altering the birefringence of a fixed thickness of a crystal such as lithium niobate. These materials are not suitable for use at millimeter and submillimeter wavelengths, currently leaving only the cumbersome approach of beam-splitters and variable delay lines. However, subwavelength artificial dielectric gratings can be made to exhibit strong birefringence, providing a fast, compact and low-cost alternative to devices such as box prisms in communications and instrumentation applications.

Artificial dielectrics are best known for their antireflection (AR) properties, both in the visible [12]–[14] and at millimeter and submillimeter wavelengths [15], [16]. The variable artificial dielectric retarder (VADR) device was recently proposed for use at terahertz frequencies [17] and initial experiments have demonstrated the device's principle of operation at 100 GHz [18], with a measured retardance of up to 74°.

In this paper, we present a thorough explanation and evaluation of the investigation of the VADR device. New measurement data is included, showing the wide bandwidth of the VADR device, due to the deep subwavelength features employed. Further simulations have been performed to investigate improvements. The addition of quarter-wave dielectric AR coatings to the exterior of the device will significantly reduce the insertion loss. Alternative geometries, such as rectangular groove gratings, are investigated in the context of single and double grating devices. Both devices show improved performance with the single grating device capable of 90° retardance, and the double grating device capable of 180°. A retardance of up to 180° is required for full polarization control.

The paper is presented in the following order. The theoretical and experimental investigations of the VADR device are described next. Both the simulated and measured results, along with the additional measured data on the bandwidth of the device, are presented and discussed in Section III. Improvements to the VADR device are presented and discussed in Section IV. Conclusions are presented in Section V.
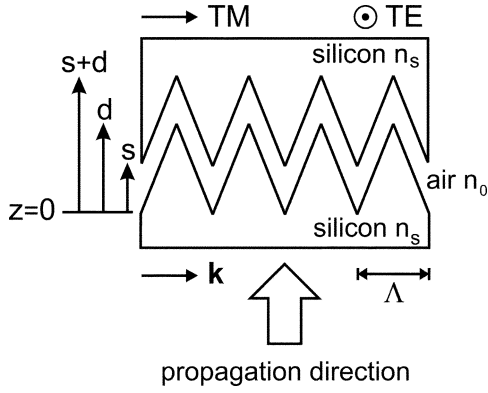
Fig. 1. Variable artificial dielectric retarder (VADR) device in cross section. The device is made from two V-grooved substrates with refractive index n_s, groove depth d, groove period Λ (grating vector **k**), and separation s.

II. INVESTIGATION OF THE VADR

We investigated the properties of a silicon VADR device at 100 GHz, both theoretically and experimentally. In the first part of this section, the operation of the VADR device is explained using an effective medium theory (EMT). Due to the limitations of the EMT analysis, the use of a numerical technique is required for comparison to the experiment. In the second part of this section, the fabrication of the VADR device using conventional silicon micromachining techniques is described, along with the free-space measurement setup at 100 GHz and the experimental procedure.

A. Theoretical

The geometry of the silicon VADR device is shown in the cross section of Fig. 1, for the case where the two identical interlocking subwavelength gratings on the interior surfaces are of the V-groove form. The V-groove nature of the grating is not essential, nor is the substrate material; we have studied the silicon V-groove grating device because of silicon's high refractive index ($n_s = 3.42$) and the convenience in fabrication afforded by conventional silicon bulk micromachining techniques. The transverse electric (TE) and transverse magnetic (TM) electric field directions are defined with respect to the grating vector **k**, s is the separation between the plates, Λ is the period and d is the groove depth. For the device investigated here, $\Lambda = 500~\mu m$, $d = 350~\mu m$, and at 100 GHz the free space wavelength is $\lambda_0 = 3$ mm and the wavelength in the silicon substrate is $\lambda_s = \lambda_0/n_s = 0.877$ mm.

As the grating period is subwavelength ($\Lambda < \lambda_s$) the retardance of the VADR device (defined here as the absolute phase shift between TE and TM polarizations that is induced by propagation through the device) can be calculated in the first instance using effective medium theory (EMT). EMT may be used to model periodic structures, such as gratings, as homogeneous layers with anisotropic properties. In the zeroth-order EMT approximations [12] the effective refractive indices for TE and TM polarizations at any depth z are

$$n_{TE}(z) = n_s F(z) + n_0 (1 - F(z)) \tag{1a}$$

$$n_{TM}(z) = \left[\frac{F(z)}{n_s} + \frac{1 - F(z)}{n_0} \right]^{-1} \tag{1b}$$

where $F(z)$ is the fill factor of the structure at depth z. For the VADR device shown in Fig. 1, in the region of the grooves, the fill factor is

$$F(z) = \begin{cases} 1 - \frac{z}{d}, & \text{for } 0 \leq z < s \\ 1 - \frac{s}{d}, & \text{for } s < z \leq d \\ 1 - \frac{z-s}{d}, & \text{for } d < z \leq s+d \end{cases} \tag{2}$$

In the unpatterned substrate $F(z) = 1$ so $n_{TE} = n_{TM} = n_s$, and in the air outside the device $F(z) = 0$ so $n_{TE} = n_{TM} = 1$. Note that in the region of the grooves (1) gives rise to unequal TE and TM refractive indexes, hence, the birefringence property that is desired.

The birefringence of the VADR device can be calculated approximately as follows. The averaged propagation constant that is used to determine the device's phase shift in each region is

$$k_{u,v} = \frac{k_0}{v - u} \int_u^v n(z) dz \tag{3}$$

where v and u define the boundaries of the portion of the artificial dielectric concerned, and k_0 is propagation constant of free space. When $s < d$ the overall phase retardance Γ between the TM and TE polarized electric fields can be calculated to be

$$\Gamma_{s<d}(s) = \left(k_{0,s}^{TM} - k_{0,s}^{TE} \right) s + \left(k_{s,d}^{TM} - k_{s,d}^{TE} \right) (d - s) + \left(k_{d,s+d}^{TM} - k_{d,s+d}^{TE} \right) s \tag{4}$$

by accumulating the differential phase shifts in the three regions of (2).

Even in this most simple form, the analysis still captures the essence of the device's operation. When the plates are fully interlocked, there is no birefringence because the device is effectively a uniform slab of dielectric. As the plates are separated, an air gap is introduced between the two sets of grooves, allowing the artificial dielectric gratings to emerge. The total birefringence of the device increases with the plate separation distance s because the total apparent thickness of the artificial dielectric layers increases, allowing the wave to accumulate a greater phase delay between its components.

An improved model that treats the device as a Fabry-Pérot cavity with birefringent mirrors has been previously developed [17]. It accounts for the reflections between the plates, and can handle separations exceeding the groove depth. The details are not repeated here, however it predicts that once the separation distance exceeds the groove depth, the retardance oscillates as a function of separation distance. This analysis can be applied to the more accurate formulations of EMT that account for the groove period-wavelength ratio [19], and also the the groove depth-wavelength ratio [20].

Unfortunately, the EMT approximations are known to become inaccurate for materials with a high dielectric constant when the grating period approaches $\lambda_0/4$. A numerical vector Maxwell Equation solving tool, such as rigorous coupled wave analysis (RCWA), is expected to provide more accurate results because it does not rely on the simplifying assumptions of EMT. RCWA is not described here, because it has been fully described
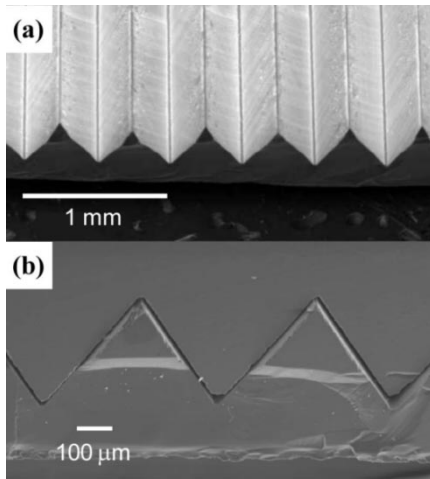
Fig. 2. Scanning electron microscope micrographs of VADR. (a) Single plate. (b) Complete device, with fully interlocked plates.

Fig. 3. Block diagram of experimental setup at 100 GHz, showing transmit horn excited in the W band by a frequency synthesizer, and the receive horn connected to a vector network analyzer. The VADR device is mounted between the horns, encompassing the beam.

elsewhere (see [21] and references therein). We used a commercial implementation of RCWA [22], to model the device for comparison with the experimentally obtained results.

For the RCWA simulations, a ten-layer staircase structure approximated the 350 μm-deep V-grooves, and the unpatterned rear section of the substrate was modeled with a further layer, 200 μm thick. The simulations modeled the interlock region ($0 \leq s < 350 \mu$m) in 35 μm steps, and the remainder ($350 < s \leq 3000 \mu$m) in 50 μm steps. The silicon substrate was modeled with complex refractive index n $= 3.42 + 0.0384$i [23], in order to suit the silicon material we used in the fabrication of our VADR device (described in the next part of this section). This figure is reliable for 200-Ω·cm silicon, but will introduce some discrepancies into our present comparison of theory and experiment since we used material with 10–20 Ω-cm resistivity. Accurate data at 100 GHz for the loss of the silicon used for our experimental devices was not available.

B. Experimental

VADR plates were fabricated with bulk micromachining techniques. A 100-mm-diameter (100)-orientation p-doped silicon wafer was coated in 200 nm of silicon nitride and cleaved into 20 mm by 22 mm samples. Special rotational alignment marks with $0.4°$ angular spacing were used in conjunction with a short pre-etch in 40% w/w potassium hydroxide (KOH) at 80 °C, to accurately define the [110] directions on the wafer. The silicon nitride on each sample was reactive ion etched (RIE) to form a linear grating of period 500 μm and linewidth 40 μm. The mask was aligned with the indicated [110] directions in order to avoid excessive undercutting during groove formation. The grooves were formed by etching each plate in the same KOH solution as before, for 280 min. The KOH solution etched vertically at 1.2 μm/min, but was prevented from etching laterally by the {111} etch stop planes that extend from the mask edges at an angle of $54.7°$ to the surface [24]. These etch stop planes formed the sloping sidewalls of the V-grooves, as shown in the scanning electron microscope (SEM) micrographs of Fig. 2, with a single VADR plate in Fig. 2(a) and a completed VADR device comprising
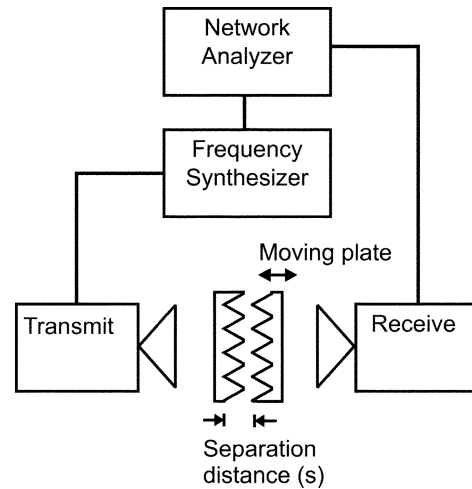
two interlocked plates in Fig. 2(b). The silicon nitride was removed in buffered 40% w/w hydrofluoric acid.

A VADR device was assembled from two such silicon plates, and characterized in the W band (70–110 GHz). The setup presented in Fig. 3 was used to measure the phase and magnitude of the scattering parameters for both TE and TM polarizations at frequencies between 70 and 110 GHz, in order to quantify the desired retardance and the insertion loss of the device. The transmitting pyramidal horn antenna was excited by a synthesized sweeper and up-converter to produce -15 dBm in the W band. A vector network analyzer measured full S-parameters. The transmit and receive horns were separated as widely as possible within the constraints of the equipment, by approximately 25λ, to ensure as planar wavefront as possible at the device.

Several steps were taken to ascertain the reliability of the measurements. Using a separate setup that allowed the receive horn to rotate, we measured the extinction ratio of the horns to be in excess of 32 dB, the value being limited by the source-power and noise floor of that measurement. The E- and H-plane beam patterns of the horn were semianalytically calculated after the method of [25]. With the exposed device area being 20 mm by 20 mm, located approximately 37 mm from the horn, it was expected that the device would encompass the emitted beam out to -11 dB in the E plane, and -13 dB in the H plane. The difference in values arises because the beam is slightly wider in the E plane. The entire setup, minus only the VADR device itself, was measured across the range of positional settings. The transmission magnitude was -8.7 ± 0.1 dB, and the phase was $3.2 \pm 0.6°$. Two plain silicon plates of the same dimensions as the VADR device were also measured across the range of the positional settings. They showed the expected Fabry-Pérot cavity behavior, with the transmission magnitude varying from -11 to -18.5 dB (with the insertion loss of the holders removed) and the phase varying across a range of $15°$. The plates were also rotated through $90°$, and remeasured. Since plain silicon substrates have no polarizing properties, the rotation of the plates did not change their behavior. This was important because it showed that any difference in the measurements as a result of
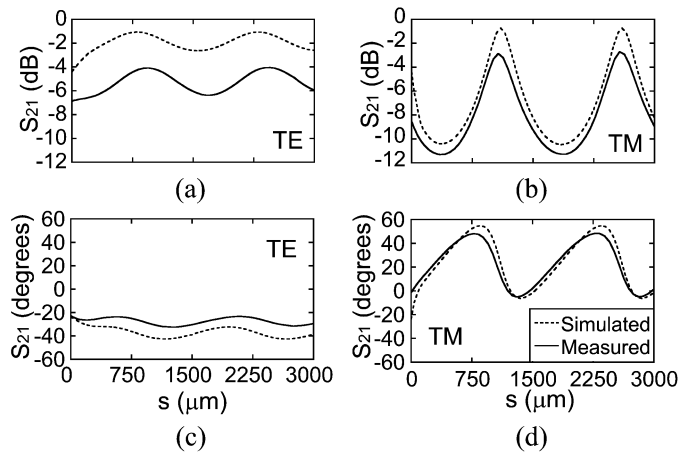
Fig. 4. Complex transmission coefficients of the VADR variable polarization compensator for incident TE and TM linearly polarized radiation at 100 GHz. (a) TE magnitude. (b) TM magnitude. (c) TE phase. (d) TM phase. Solid lines: measured data with 8.7 dB test fixture insertion loss removed. Dashed lines: RCWA simulated data.

Fig. 5. VADR retardance as a function of plate separation $\Gamma(s)$ at 100 GHz. Solid line: measured data. Dashed line: RCWA simulated data.

changing the orientation of the VADR plates, was attributable only to the birefringent nature of the VADR device's subwavelength gratings.

The VADR plates were fixed over fiberglass apertures with double-sided adhesive foam for mechanical cushioning at full interlock. One holder was fixed in position and the other one was mounted on a micrometer-driven translation stage to control the separation distance. The outside of each aperture was covered with microwave absorbing foam to reduce field leakage. Metal surfaces were similarly covered to reduce stray reflections.

For the TM measurement, the plates were mounted with **k** parallel to the electric field. The plate separation distance was set at one free space wavelength (3 mm) and reduced in 60 μm steps until the grooves just reached the interlock region (< 350 μm). Since the sensitivity of the device was greater in the interlock region, the separation distance was reduced with a step size of 20 μm until full interlock was reached (0μm). The plates were remounted with **k** perpendicular to the electric field for the TE measurement. The measurement steps were repeated. At each separation, the S-parameters were recorded for 256 frequencies between 70 and 110 GHz.

III. RESULTS AND DISCUSSION

The complex transmission coefficients for the design frequency of 100 GHz are plotted as solid lines for measured data and dashed lines for RCWA simulated data in Fig. 4, with TE magnitude in Fig. 4(a), TM magnitude in Fig. 4(b), TE phase in Fig. 4(c) and TM phase in Fig. 4(d). Note that the measured phase is raw data, but the measured magnitude data has the test fixture's insertion loss (8.7 dB) removed. The measured curves show two distinct regions of operation, one corresponding to interlocked plates (0–350 μm), the other separated plates (> 350 μm). In the separation region, Fabry-Pérot cavity oscillations are evident, with a period of half the free-space wavelength. The magnitude responses, Fig. 4(a) and (b), are different for TE and TM due to the birefringent grooves. Over the entire operating range, the insertion loss oscillates from 4–7 dB for TE and 3–11 dB for TM radiation. The phase re-
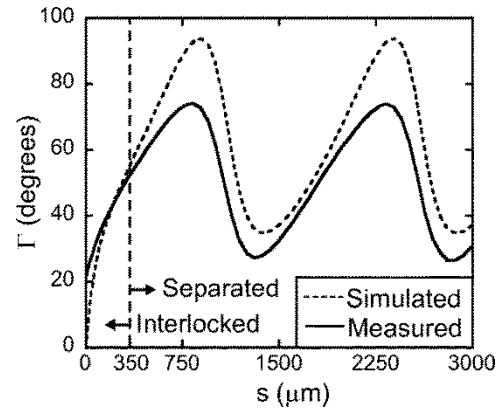
sponse also differs between TE and TM, oscillating from $-20°$ to $-30°$ for TE, and $0–50°$ for TM radiation. The simulations correctly predict the shape of the oscillation in the phase of the TM response, the relative magnitudes of the oscillations in both phase and magnitude responses, and the positions of the peaks and troughs of those oscillations (see Fig. 4). Quantitatively, the measured and simulated results for the TM polarization agree within 2 dB and 10° for magnitude and phase, respectively, while the TE polarization shows discrepancies of up to 4 dB and 11°. The differences between the experimental and simulated data arise from the finite size of the test structure, resulting in field leakage.

The difference in the phase response between TE and TM polarizations is the birefringence property that is desired, and this is plotted in Fig. 5 with a solid line for the measured retardance, and a dashed line for the simulated retardance. This gives a measure of the device's retardance as a function of the plate separation, $\Gamma(s)$. The maximum retardance of 74° is approaching a quarter wave, and was measured at a separation of 830 μm. There are two distinct areas of quasilinear variation in $\Gamma(s)$. The first is in the interlock region, where separation distance is less than the groove depth (0–350 μm). The retardance changes from 22° to 34°, for separation distances 0–100 μm, yielding a sensitivity of 120°/mm. A 0° retardance was not observed due to mechanical imperfections inhibiting full interlock. Fig. 2(b) shows a device in full interlock having a plate separation of 20 μm, resulting from surface irregularities. A second region of quasilinear variation occurs for separations of 1000–1300 μm, giving a relative change in retardance of 36°, and sensitivity of $-120°$/mm. Note that this is in the separation region, where the birefringent–mirror Fabry-Pérot behavior dominates. According to the simulations, the peak retardance is 93° at a separation of 880 μm; with a relative change of 29°, the maximum sensitivity is 290°/mm for separation distances 0–100 μm, and with a relative change of $-51°$, the sensitivity is $-170°$/mm for separations 1000–1300 μm. Note that these differences are a result of the previously identified discrepancies in the phase of the measured and simulated complex transmission coefficients.

The frequency-dependence of the device has also been characterized by measurement. The retardances at the upper (110 GHz) and lower (70 GHz) ends of the measurement range
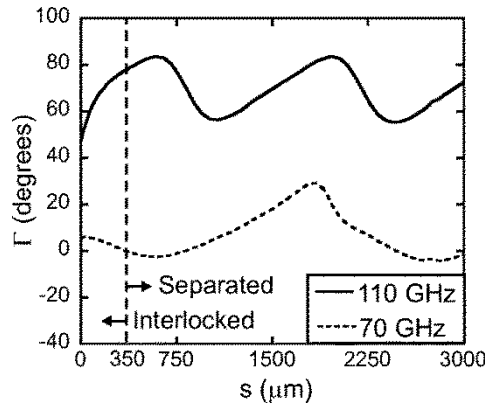
Fig. 6. VADR retardance $\Gamma(s)$ measured at the upper (110 GHz) and lower (70 GHz) ends of the W band range.

are shown in Fig. 6. For the 110 GHz trace, there is shown a full period of the separation-region oscillation. The period of the oscillation corresponds to half the free space wavelength, $\lambda_0/2 = 1.35$ mm, as would be expected from a Fabry-Pérot cavity. The effective groove depth (the groove depth divided by the free space wavelength) decreases at lower frequencies, lowering the effective path difference between the TE and TM polarizations. Consequently, there is a reduction in the peak retardance and sensitivity at 70 GHz, and the position of peak retardance moves to greater separation distances. It is seen from these measurements that the device operation is dispersive, but it operates as a variable polarization compensator over a wide bandwidth, and the sensitivity increases with frequency.

IV. IMPROVEMENTS ON VADR

Because the simulations agree well with experiment, we have confidence in the use of the RCWA simulation technique for the design of improved VADR devices. This is important, since the 3–11 dB insertion losses for the VADR devices fabricated to date are larger than would be acceptable for many practical applications. A more acceptable figure for the maximum insertion loss of this type of device is in the range 0.1–1 dB. Additionally, the current retardance is sufficient for correcting deviations from a given polarization state, but a retardance of at least 90° (quarter-wave) is required for basic polarization transformations such as linear to circular. A retardance of 180° (half-wave) is required for full polarization control, including the rotation of linear polarizations. Specific applications may require additional criteria such as a linear variation in retardance with separation, closely matched TE and TM insertion losses, or high sensitivity.

The insertion loss is predicted to improve with the addition of quarter-wave antireflection (AR) coatings. The two exterior surfaces of the VADR device form an additional pair of strongly reflecting mirrors, due to the abrupt substrate-air interface. This results in an increase in, and a mismatch between, the TE and TM insertion losses. The required index of the AR coating is $\sqrt{n_{Si}} = 1.85$, and at 100 GHz the quarter-wave thickness is 405 μm. A suitable candidate material is SU-8 photoresist, with a refractive index of 1.8 at 100 GHz [26]. The comparison between non-AR- and AR-coated devices is made here for lossless
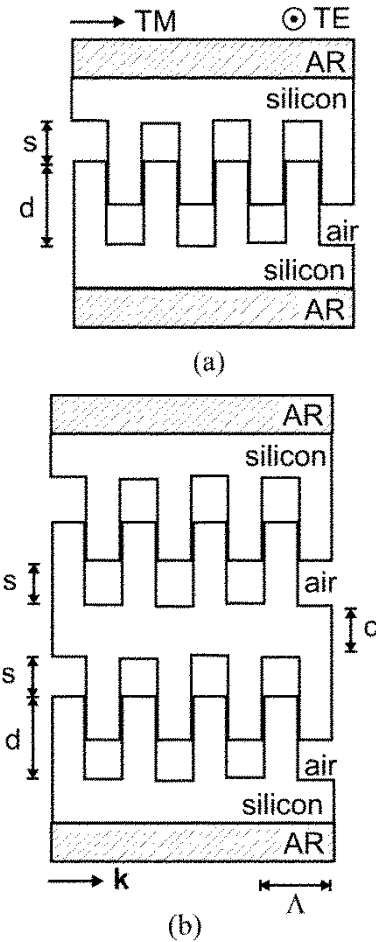

Fig. 7. Cross section of improved VADR polarization compensation devices, with plates separated, showing grating wave vector ($\mathbf{k}$), electric field TE and TM directions, groove depth d, plate separation s, center thickness c, and quarter-wave AR coatings (not shown to scale). (a) R-VADR single grating device. (b) R^2-VADR double grating device.

substrates, to show that the improvement is generally applicable, and not restricted to lossy substrates. Simulations of VADR with lossless silicon substrate $n = 3.42$ show an insertion loss of 0–4 dB for TE and 0–10 dB for TM. With the addition of the ideal AR-coatings, the insertion loss reduces to 0–3 dB for TE and 0–4 dB for TM. However, the peak retardance falls from 88 to 50°, and the sensitivity becomes 59°/mm.

A 90° retardance could still be produced by cascading two AR coated, V-grooved VADR devices in series, and 180° by using four. For practical reasons, it is preferable to use only a single device or reduce the number of devices in the cascade, by using devices with a greater retardance. For this reason, we investigated alternative grating geometries that offered greater birefringence. Simulations are presented of both single and double grating-pair devices with rectangular grooves, that we have called the R-VADR and R^2-VADR, respectively, [see Fig. 7(a), (b)]. We predict the R-VADR is capable of a quarter-wave retardance, and the R^2-VADR a half wave retardance. We find that enhanced sensitivity and reduced loss is obtained with rectangular-grooved structures compared to the equivalent VADR structures. Hence, no further simulations are presented for V-grooved devices. Due to the improved insertion loss, all further simulations include the quarter wave dielectric AR coating.

TABLE I
CHARACTERISTICS OF THE R-VADR RETARDANCE $\Gamma(s)$ FOR VARIOUS GROOVE DEPTHS AT 100 GHz

Groove depth d (μm)	Peak retardance (degrees)	Separation at peak retardance (μm)	Total sensitivity (degrees/mm)	Insertion loss (TE, dB)	Insertion loss (TM, dB)
200	54	800	67	$0 - 2.8$	$0 - 3.6$
350	112	750	150	$0 - 2.6$	$0 - 2.0$
500	147	850	173	$0 - 5.0$	$0 - 5.0$

A. R-VADR

The R-VADR differs from the previously investigated VADR only in that the grooves are rectangular. The basic theory of operation remains the same, but we find the increased birefringence of the rectangular grooves provides a greater retardance.

The rectangular cross-sectional geometries required for R-VADR can be made using deep reactive ion etching (DRIE) micromachining techniques for short operating wavelengths where groove depths up to approximately 300 μm are required [27]. For deeper grooves at short operating wavelengths, excimer laser ablation may be used; for longer operating wavelengths, the lateral feature sizes are large enough for mechanical cutting techniques to be used. It would be possible to fabricate plates from alternative materials, and molding could be used for mass production. All four techniques allow the depth to be controlled precisely, and the groove depth to be chosen to be any value without the restrictions imposed by the KOH etch technique. Thus, devices of the same 500 μm period, but with three different groove depths (d), [see Fig. 7(a)], have been investigated: the direct equivalent to the VADR ($d = 350 \ \mu$m), one shallower ($d = 200 \ \mu$m) and one deeper ($d = 500 \ \mu$m). The same RCWA technique was used for these simulations as before. The retardance, total sensitivity, and insertion losses for all three R-VADR devices are tabulated in Table I. The total sensitivity is defined as the peak retardance divided by the separation at the peak retardance.

Examining Table I, it is clear that d plays a pivotal role in determining the peak retardance. We find that the greater d, the greater the peak retardance. Compared to the equivalent VADR, the 350 μm R-VADR gains 62° in peak retardance and 91°/mm in sensitivity, and the worst insertion loss is improved by 1.4 dB. The TE and TM insertion losses are also better matched; they differ by up to 0.6 dB at some separations, compared to differences of up to 1.6 dB for the VADR. The insertion losses for the other R-VADR's are slightly worse, indicating that the losses do not necessarily increase in proportion to the groove depth.

The R-VADR is easily capable of achieving a quarter-wave retardance, with an improved magnitude response compared to the VADR. The improved performance is attributed to the higher total birefringence of the rectangular gratings that now have a constant effective refractive index as a function of depth, rather than being smoothly graded as in the V-groove case.

B. R^2-VADR

A device capable of a half-wave retardance makes an attractive proposition, as this is necessary for complete polarization control. The simplest method of doubling the available peak retardance is coupling two R-VADRs in series, combining the inner two plates into a double-sided grating. We have named such a device the double rectangular groove VADR, or R^2-VADR. The behavior of an R^2-VADR is determined by both the groove depth d as for the R-VADR, but also by the thickness of the substrate between the center plate's two gratings; this is dimension c in Fig. 7(b). The substrate thicknesses on the outer plates have no effect on the performance, as the outer surfaces are AR coated. To adjust the separation distance of the R^2-VADR, the center plate is held fixed, while the two outer plates are moved by the same distance s such that they are always equidistant from the center plate. Alternatively, asymmetrical operation of this device is possible, as there are now two degrees of freedom for plate separation, but these cases are not explored here.

We selected as an example for this paper, a device with the dimensions $c = 840 \ \mu$m and $d = 730 \ \mu$m, because our investigations indicated that these dimensions gave a high retardance and a low insertion loss. RCWA simulation results at 100 GHz for the R^2-VADR device are plotted in Fig. 8, with the retardance $\Gamma(s)$ in Fig. 8(a), and the magnitudes of the TE and TM transmission coefficients in Fig. 8(b). The peak retardance is 416°, well in excess of the 180° required for full polarization control. The sensitivity over retardances 0–180° (the operating region), which correspond to separations 0–370 μm, is 485°/mm, more than three times that obtained from the original VADR device. The insertion losses in the interlocked operation region are low, at 0–0.1 dB for TE and 0–0.1 dB, except for a 0.6 dB peak at 300 μm separation, for TM. Outside the operating region, where the insertion loss is not as important, it is larger at 0–10 dB for TE and 0–5 dB for TM.

The excellent insertion loss figures for the R^2-VADR will be subject to increase in a practical device since there will be additional loss owing to absorption in the substrate, but this can be minimized by using high resistivity wafers [23]. Other practical considerations include the possibility that mechanical imperfections may prevent full interlock. Additionally, any clearance between the grooves to alleviate stiction would result in a slight, but acceptable, performance degradation. It is unfortunate that in both cases, the ability of the device to reach zero retardance would be compromised. We are currently investigating a device which overcomes these difficulties.

Piezoelectric actuators can now easily manage the relatively small shifts ($< 400 \ \mu$m) required for a half-wave device. The addition of suitable electronic control would produce a device with a small footprint, capable of modulating polarization at tens of kHz for information gathering or encoding, or providing steady state compensation.
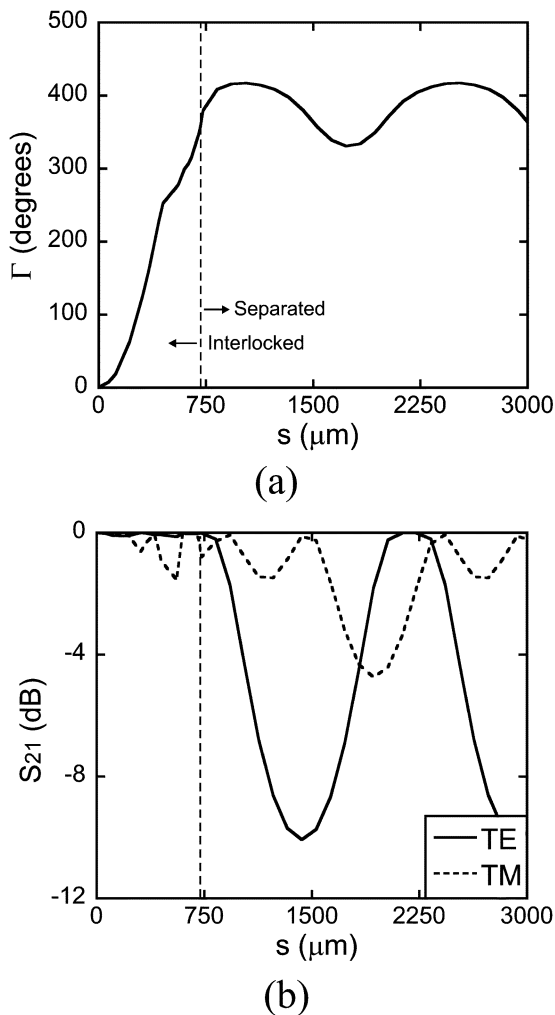
Fig. 8. Transmission characteristics at 100 GHz of the R^2-VADR device with dimensions $c = 840~\mu$m, $d = 730~\mu$m. (a) Retardance $\Gamma(s)$. (b) Magnitude of the TE and TM transmission coefficients.

low cost, electronically controlled device capable of full polarization modulation or steady state compensation at millimeter and submillimeter wavelengths.

V. CONCLUSION

A VADR using V-groove artificial dielectrics has been fabricated, tested and modeled at a frequency of 100 GHz. Variable retardances of up to 74° have been measured, in good agreement with RCWA simulations. The retardance can be greatly modified for small, easily controlled, changes in separation distance. Operation is wavelength specific, but wide bandwidth, and the fabrication process scales easily.

Further investigations into device improvements, including rectangular artificial dielectric gratings and coupled devices, have been carried out by detailed simulation. The addition of AR coatings to the two exterior surfaces of a single device reduces the insertion loss. A rectangular groove device (R-VADR) is predicted to have more than twice the sensitivity $(150°/\mathrm{mm})$ of the equivalent depth V-groove device, and is capable of quarter wave retardance. A double rectangular grating device (R^2-VADR) offers a peak retardance in excess of a half wave and eight times the sensitivity of the VADR, at less than one third of the insertion loss (0–0.6 dB). With piezoelectric actuators, the R^2-VADR would make a compact,

REFERENCES

[1] S. Hunsche, M. Koch, I. Brener, and M. Nuss, "THz near-field imaging," *Opt. Commun.*, vol. 150, no. 1–6, pp. 22–26, 1998.
[2] Z. Jiang and X.-C. Zhang, "Terahertz imaging via electrooptic effect," *IEEE Trans. Microwave Theory Tech.*, vol. 47, pp. 2644–2650, Dec. 1999.
[3] M. Gaidis, H. Pickett, C. Smith, S. Martin, R. Smith, and P. Siegel, "A 2.5-THz receiver front end for spaceborne applications," *IEEE Trans. Microwave Theory Tech.*, vol. 48, pp. 733–739, Apr. 2000.
[4] J. Kindt and C. Schmuttenmaer, "Theory for determination of the low-frequency time-dependent response function in liquids using time-resolved terahertz pulse spectroscopy," *J. Chem. Phys.*, vol. 110, no. 17, pp. 8589–8596, 1999.
[5] D. S. Citrin, "Optical analogue for phase-sensitive measurements in quantum-transport experiments," *Phys. Rev. B*, vol. 60, no. 8, pp. 5659–5663, Aug. 1999.
[6] P. Bondavalli, R. LeDantec, and T. Benyattou, "Influence of the involuntary underetching on the mechanical properties of tunable Fabry—Pérot filters for optical communications," *J. Microelectromech. Syst.*, vol. 10, no. 2, pp. 298–301, 2001.
[7] S. Yao, "Controlling polarization-related impairments," *Laser Focus World (WDM Solutions Supplement)*, vol. 36, no. 11, pp. 63–72, Nov. 2000.
[8] M. Andrews, P. Mitra, and R. deCarvalho, "Tripling the capacity of wireless communications using electromagnetic polarization," *Nature*, vol. 409, pp. 316–318, Jan. 2001.
[9] E. Dietrich, B. Enning, R. Gross, and H. Knupke, "Heterodyne transmission of a 560 Mbit/s optical signal by means of polarization shift keying," *Electron. Lett.*, vol. 23, no. 8, pp. 421–422, 1987.
[10] R. Blaikie, D. Taylor, and P. Gough, "Multilevel differential polarization shift keying," *IEEE Trans. Commun.*, vol. 45, pp. 95–102, 1997.
[11] *Handbook of Optics*, W. G. Driscoll, Ed., McGraw-Hill, New York, 1978.
[12] D. Raguin and G. Morris, "Analysis of antireflection-structured surfaces with continuous one-dimensional surface profiles," *Appl. Opt.*, vol. 32, no. 14, pp. 2582–2598, 1993.
[13] A. Parker, "Light-reflection strategies," *Amer. Scientist*, vol. 87, no. 3, pp. 248–255, 1999.
[14] B. Macleod and G. Sonek, "Motheye surfaces reflect little light," *Laser Focus World*, vol. 35, no. 8, pp. 109–114, 1999.
[15] T. Kononenko, V. Kononenko, V. Konov, S. Pimenov, S. Garnov, A. Tishchenko, A. Prokhorov, and A. Khomich, "Formation of antireflective surface structures on diamond films by laser patterning," *Appl. Phys. A*, vol. 68, no. 1, pp. 99–102, 1999.
[16] S. Gloor, V. Romano, W. Lüthy, H. Weber, V. Kononenko, S. Pimenov, V. Konov, and A. Khomich, "Antireflection structures written by excimer laser on CVD diamond," *Appl. Phys. A*, vol. 70, no. 5, pp. 547–550, 2000.
[17] D. Cumming and R. Blaikie, "A variable polarization compensator using artificial dielectrics," *Opt. Commun.*, vol. 163, pp. 164–168, May 1999.
[18] T. Drysdale, H. Chong, R. Blaikie, and D. Cumming, "Variable polarization compensator using artificial dielectrics for millimeter and sub-millimeter waves," *Electron. Lett.*, vol. 37, no. 3, pp. 149–150, Feb. 2001.
[19] S. Rytov, "Electromagnetic properties of a finely stratified medium," *Soviet Phys. JETP*, vol. 2, no. 3, pp. 466–475, May 1956.
[20] P. Lalanne and D. Lemercier-Lalanne, "Depth dependence of the effective properties of subwavelength gratings," *J. Opt. Soc. Amer. A*, vol. 14, no. 2, pp. 450–458, Feb. 1997.

[21] M. Moharam, D. Pommet, E. Grann, and T. Gaylord, "Stable implementation of the rigorous coupled-wave analysis for surface-relief gratings: enhanced transmittance matrix approach," *J. Opt. Soc. Amer. A*, vol. 12, no. 5, pp. 1077–1086, May 1995.

[22] Gsolver4.12, Grating Solver Development Company, Allen, TX 75013.

[23] M. Afsar, I. Tkachov, and K. Kocharyan, "Quasioptical waveguide W band spectrometer for precision dielectric measurement of absorbing materials," in *Proc. IEEE Conf. Precision Electromagnetic Measurements*, Washington, DC, July 1998, pp. 530–531.

[24] E. Bassous, "Fabrication of novel three-dimensional microstructures by the anisotropic etching of (100) and (110) silicon," *IEEE Trans. Electron Devices*, vol. ED-25, pp. 1178–1185, 1978.

[25] C. Balanis, *Antenna Theory: Analysis and Design*, Singapore: Wiley, 1982.

[26] S. Arscott, F. Garet, P. Mounaix, L. Duvillaret, J.-L. Coutaz, and D. Lippens, "Terahertz time-domain spectroscopy of films fabricated from SU-8," *Electron. Lett.*, vol. 3, pp. 243–244, 1999.

[27] T. Pandhumsoporn, M. Feldbaum, P. Gadgil, M. Puech, and P. Maquin, "High-etch-rate, anisotropic deep silicon plasma etching for the fabrication of microsensors," in *SPIE Proc. Micromachining and Microfabrication Process Technology II*, vol. 2879, 1996, pp. 94–102.

Richard J. Blaikie (M'95) received the B.Sc. (Hons.) degree from the University of Otago, New Zealand, in 1988 and the Ph.D. degree in physics from the University of Cambridge, U.K., in 1992.

For one year, he was a Visiting Scientist at the Hitachi Cambridge Laboratory, investigating single-electron transport effects in semiconductors. He returned to New Zealand in 1993, taking up a position as a Postdoctoral Research Fellow with the Department of Electrical and Computer Engineering, University of Canterbury. In 1994, he was appointed to his current faculty position within this department. His research interests include the fabrication of semiconductor nanostructures, polarization effects in free space and optical fiber communications systems, and modeling of semiconductor devices.

Dr. Blaikie is a Member of the Institute of Physics.

Harold M. H. Chong was born in Brunei in 1974. He received the B.Eng.(Hons) and M.Sc. degrees from the University of Glasgow, U.K., in 1997 and 2002, respectively, where he is currently working toward the Ph.D. degree in photonic wire waveguides and photonic crystals.

His research interests are photonic crystals for millimeter-wave and optoelectronic applications and photonic integrated circuits.

Timothy D. Drysdale was born in New Zealand in 1977. He received the B.E. (Hons.) degree (1st class, University Prize) in electrical and electronic engineering from the University of Canterbury, New Zealand, in 1998, where he is working toward the Ph.D. degree on the subject of passive devices for terahertz frequencies.

He then joined the Nanostructure Engineering, Science and Technology Research Group of the University of Canterbury. In May 2002, he moved to the U.K. to become a research assistant with the Department of Electronics and Electrical Engineering, University of Glasgow, Glasgow, U.K..

David R. S. Cumming (M'97) received the B.Eng. and Ph.D. degrees from the University of Cambridge, Cambridge, U.K., in 1989 and 1993, respectively.

He has worked variously on mesoscopic device physics, RF characterization of novel devices, fabrication of diffractive optics for optical and sub-millimeter wave applications, and microelectronic design. He is presently a Senior Lecturer and EPSRC Advanced Research Fellow with the Department of Electronics and Electrical Engineering, University of Glasgow, Glasgow, U.K., where he leads the Microsystem Technology Group.